Acta Mechanica 106, 87–105 (1994)

ACTA MECHANICA

Effect of frictional force and nose shape on axisymmetric deformations of a thick thermoviscoplastic target

R. C. Batra and **X. Chen**, Rolla, Missouri

(Received January 4, 1993)

Summary. We study thermomechanical deformations of a thermally softening viscoplastic thick target impacted at normal incidence by a cylindrical rod made of a material considerably harder than the target material. Thus we regard the penetrator to be rigid and analyze the effect of the penetrator nose shape and the frictional force at the target/penetrator interface on target's deformations. In the postulated expression for the frictional force, the coefficient of friction, defined as the ratio of the tangential force at a point to the normal force there, is a function of the relative speed of sliding between the two bodies. The computed depth of penetration is found to match very well with that observed in experiments by Forrestal et al. For each nose shape studied, the consideration of frictional forces reduces significantly the computed penetration depth. For the same kinetic energy of the penetrator, the penetrator with a sharp nose gives higher values of the penetration depth as compared to that obtained with a blunt nose.

1 Introduction

In many penetration problems one will like to determine as accurately as possible the resisting force experienced by the penetrator. This force decelerats the penetrator and thus influences the depth of penetration and target's deformations. Whereas a significant part of this resisting force is due to the hydrostatic pressure in the deforming target region ahead of the penetrator nose, the frictional force at the target/penetrator interface contributes to it too. Longcope and Forrestal [1] and Forrestal [2] have studied the effect of sliding friction in geological targets penetrated by rigid rods and modelled the frictional force by the Coulomb law with constant coefficient of friction. These authors used the cavity expansion method to analyze the problem. Chen [3] employed the finite element method to study the same problem, and assumed that the coefficient of friction in the Coulomb law depended upon the relative speed of sliding between the two surfaces. Recently Chen and Batra [4] proposed a different expression for the velocity dependent coefficient of friction, and determined the two constants in that expression by ensuring that the distribution of the frictional force on the hemispherical nose surface of the penetrator obtained from a solution of the penetration problem matched well that with found by modelling the steady state penetration process as a viscous fluid flowing around the rigid penetrator. Here we use their expression for the frictional force to analyze its effect on the transient problem involving the penetration of a steel cylindrical rod impacting at normal incidence a thick aluminum target. We also study the effect of the nose shape on the deformations of the target.

Forrestal et al. [5] have described a series of tests involving the penetration of steel rods into aluminum targets. They reported only the depth of penetration and observed that the steel rod stayed undeformed for all practical purposes. Here we take the penetrator to be rigid and give details of the deformation fields such as history of the temperature at a material point, history of the penetrator speed, and the distribution of the temperature and velocity field in the deforming target region. For the sixteen tests simulated herein, the computed depth of penetration has been found to match very well with that reported by Forrestal et al. [5].

We refer the reader to the review articles by Backman and Goldsmith [6], Wright and Frank [7], Anderson and Bodner [8], and the books by Zukas et al. [9], Blazynski [10], MaCauley [11], and Zukas [12] for a summary of the available literature on ballistic penetration. Awerbuch and Bodner [13], Ravid and Bodner [14], Ravid et al. [15], Forrestal et al. [16], and Batra and Chen [17] have proposed engineering models of different complexity in which a rigid penetrator impacts a deformable terget. Batra [18] has pointed out that the target deformations during the steady state phase of the penetration process are influenced strongly by the penetrator nose shape. He assumed the target/penetrator interface to be smooth. Here we also investigate the effect of the nose shape on transient deformations of the target and account for the effect of the frictional force at the interface. The shapes of the intensely deforming target material ahead of the penetrator nose for ellipsoidal and blunt nosed penetrators are quite different. In each case the plastic deformations of the target material are large enough to melt a thin layer of the target material adjoining the target/penetrator interface.

2 Formulation of the problem

In order to keep the paper self-contained we summarize below the pertinent equations. We presume that target deformations are axisymmetric, and use a fixed set of cylindrical coordinates with z-axis coincident with the axis of symmetry and pointing into the target and the origin at the top surface of the undeformed target to describe its deformations. The balance laws written in the referential description of motion and governing the thermomechanical deformations of the target are

$$(\varrho J) = 0, \tag{1.1}$$

$$\varrho_0 \dot{\boldsymbol{v}} = \mathrm{Div}\, \boldsymbol{T}, \tag{1.2}$$

$$\varrho_0 \dot{e} = -\mathrm{Div}\, \boldsymbol{Q} + tr\, (\boldsymbol{T}\dot{\boldsymbol{F}}^T), \tag{1.3}$$

where

$$J = \det \boldsymbol{F}, \qquad \boldsymbol{F} = \mathrm{Grad}\, \boldsymbol{x}, \tag{2}$$

$\boldsymbol{x}$ is the present position of a material particle that occupied place $\boldsymbol{X}$ in the reference configuration, ϱ its present mass density, ϱ_0 its mass density in the reference configuration, $\boldsymbol{v}$ the present velocity of a material particle, $\boldsymbol{T}$ the first Piola-Kirchhoff stress tensor, $\boldsymbol{e}$ the specific internal energy, $\boldsymbol{Q}$ the heat flux per unit reference area, a superimposed dot indicates the material time derivative, and operators Grad and Div signify the gradient and divergence of field quantities defined in the reference configuration. The balance laws (1.1)–(1.3) are supplemented by the following constitutive relations:

$$\boldsymbol{\sigma} = -p(\varrho)\, \mathbf{1} + 2\mu \boldsymbol{D}, \qquad \boldsymbol{T} = \frac{\varrho_0}{\varrho}\, \boldsymbol{\sigma}(\boldsymbol{F}^{-1})^T, \tag{3.1,2}$$

$$2\mu = \frac{\sigma_0}{\sqrt{3}I}\left(\frac{\psi}{\psi_0}\right)^n (1 + bI)^m (1 - \nu\theta), \tag{3.3}$$

$$2\boldsymbol{D} = \text{grad } \boldsymbol{v} + (\text{grad } \boldsymbol{v})^T, \quad \tilde{\boldsymbol{D}} = \boldsymbol{D} - \frac{1}{3}(tr\boldsymbol{D})\,\mathbf{1}, \tag{3.4, 5}$$

$$2I^2 = tr(\tilde{\boldsymbol{D}}^2), \tag{3.6}$$

$$p(\varrho) = A\left(\frac{\varrho}{\varrho_0} - 1\right) + B\left(\frac{\varrho}{\varrho_0} - 1\right)^2, \tag{3.7}$$

$$\boldsymbol{Q} = -k\frac{\varrho_0}{\varrho}\text{grad } \theta(\boldsymbol{F}^{-1})^T, \tag{3.8}$$

$$\dot{e} = c\dot{\theta} + \dot{\varrho}p(\varrho)/\varrho^2, \tag{3.9}$$

$$\dot{\psi} = \frac{tr(\boldsymbol{\sigma D})}{\sigma_0\left(\frac{\psi}{\psi_0}\right)^n}. \tag{3.10}$$

Here $\boldsymbol{\sigma}$ is the Cauchy stress tensor, σ_0 the yield stress of the target material in a quasistatic simple tension or compression test, ψ_0 the strain at yield, n the strain hardening exponent, ν the coefficient of thermal softening, θ the temperature rise of a material particle, A may be thought of as the bulk modulus of the target material, B the second-order bulk modulus, k the thermal conductivity, and c the specific heat. The internal variable ψ may be associated with an equivalent plastic strain; its evolution is given by Eq. (3.10).

Batra and co-workers [18]–[23] have used the aforestated constitutive relations with $(\psi/\psi_0)^n$ in Eqs. (3.3) and (3.10) replaced by $(1 + \psi/\psi_0)^n$ to study the steady state penetration problem, a transient penetration problem involving a hemispherical nosed penetrator and smooth target/penetrator interface, and the initiation and growth of shear bands in a thermally softening viscoplastic material.

Recalling that the rigid penetrator moves along the z-axis, its equation of motion can be written as

$$M\dot{v}_z^P = -F_z, \tag{4.1}$$

$$F_z = \int \left(\boldsymbol{f}_t \cdot \hat{\boldsymbol{e}}_z + f_n(\hat{\boldsymbol{e}}_z \cdot \boldsymbol{n})\right) dA, \tag{4.2}$$

$$f_n = \boldsymbol{n} \cdot \boldsymbol{\sigma n}, \quad \boldsymbol{f}_t = -\mu\bar{v}^\beta(f_n)\,\boldsymbol{e}_v, \quad \boldsymbol{e}_v = \boldsymbol{v}^R/v^R, \tag{4.3–5}$$

$$\bar{v} = \left[\left(\frac{v_r}{v_z^P}\right)^2 + \left(\frac{v_z}{v_z^P}\right)^2\right]^{1/2}, \quad \boldsymbol{v}^R = \boldsymbol{v} - \boldsymbol{v}_z^P, \tag{4.6, 7}$$

where v_z^P is the speed of the penetrator in the z-direction, μ and β are constants, $\hat{e}_z$ is a unit vector in the z-direction, M is the mass of the penetrator, and the integration in Eq. (4.2) is over the target/penetrator interface. By requiring that the distribution of the frictional force on the hemispherical nose of the penetrator in a steady state penetration process matches quantitatively and qualitatively with that obtained by modelling the deforming target material as a viscous fluid flowing around the penetrator, Chen and Batra [4] obtained $\mu = 0.12$ and $\beta = 1.5$.

We assume that the target is initially at rest, is stress-free, has a uniform mass density ϱ_0 and a uniform temperature θ_a. The initial velocity of the rigid penetrator is v_0 in the positive

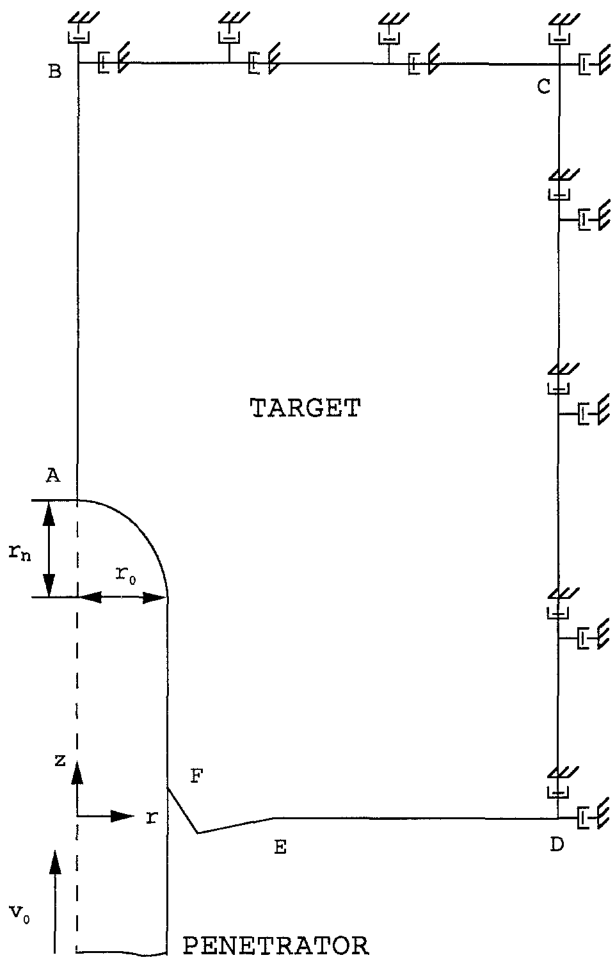

Fig. 1. A schematic sketch of the problem studied

z-direction, and we reckon time from the instant it impacts the top surface of the target at normal incidence.

In order to solve the problem numerically we analyze deformations of the finite target region ABCDEFA shown in Fig. 1 and impose the following boundary conditions on the bounding surfaces:

$$\boldsymbol{\sigma n} = \boldsymbol{0}, \quad \boldsymbol{q} \cdot \boldsymbol{n} = h(\theta - \theta_a) \quad \text{on FED,} \tag{5.1, 2}$$

$$\sigma_{rz} = 0, \quad v_r = 0, \quad q_r = 0 \quad \text{on the axis of symmetry AB,} \tag{5.3–5}$$

$$\boldsymbol{q} \cdot \boldsymbol{n} = 0, \quad \boldsymbol{\sigma n} = \boldsymbol{0} \quad \text{at a point on AF where the penetrator surface is not in contact with the deforming target region,} \tag{5.6, 7}$$

$$\boldsymbol{q} \cdot \boldsymbol{n} = 0, \quad [\boldsymbol{v} \cdot \boldsymbol{n}] = 0, \quad \boldsymbol{e}_v \cdot \boldsymbol{\sigma n} = -f_t, \quad \text{at points on AF where the penetrator and target surfaces are in contact with each other,} \tag{5.8–10}$$

$$f_n = -\varrho V_p v_n, \quad f_t = -\varrho V_s v_t, \quad \boldsymbol{q} \cdot \boldsymbol{n} = 0, \quad \text{on the bounding surface BCD.} \tag{5.11–13}$$

Here V_p and V_s are the speeds in the target material of the p-waves and s-waves, respectively, v_n and v_t are the normal and tangential components of the velocity of a target particle on the bounding surface BCD, and f_n and f_t equal, respectively, the normal and tangential forces exerted on the target particle to which the dashpot is attached. Lysmer and Kuhlemeyer [24] proposed that such dashpots when attached to the bounding surfaces will absorb the incident p- and s-elastic waves, and thus enable the replacement of an infinite region by a finite region. For the viscoplastic problem being studied herein, these dashpots will absorb some of the incident energy. The PRONTO2D code employed by Chen [3] also has non-reflecting boundaries. In Eqs. (5.1) through (5.13), $\boldsymbol{q}$ is the heat flux measured per unit area in the present configuration, h the heat transfer coefficient between the target material and the air, $[\boldsymbol{v} \cdot \boldsymbol{n}]$ indicates the jump of the normal velocity across the target/penetrator interface, and its null value ensures that there is no interpenetration of the target material into the penetrator and vice versa.

3 Numerical results and discussion

The finite element based computer code developed by Chen and Batra [4] used to analyse a penetration problem similar to the aferostated one but with a smooth target/penetrator interface and a hemispherical nosed penetrator was modified to include frictional force at the interface and different shapes of the penetrator nose. We recall that the contact conditions at the target/penetrator interface are accounted for by using the slideline algorithm due to Hallquist et al. [25]. The code employs the lumped mass matrix obtained by the row-sum technique, uses three quadrature points to numerically integrate various quantities over a triangular element, does not use any artificial viscosity in the problem formulation, and uses the explicit forward-difference method to integrate with respect to time t the coupled nonlinear ordinary differential equations obtained by applying the Galerkin approximation [26] to the governing partial differential equations. Since the forward-difference method is conditionally stable for linear problems, the time step size is controlled by the Courant condition. Here we also require that the time step be small enough so that no more than one target node not already on the target/penetrator interface comes into contact with that surface during that time interval. After every time increment, the coordinates of nodes are updated and the finite element mesh refined even if only one element has been excessively distorted (e.g. see Chen and Batra [4]). In the newly generated mesh the area of an element is inversely proportional to the value at its centroid of the second invariant of the deviatoric strain-rate tensor except that an altitude of every element is greater than 0.15 r_0 and less than $2r_0$, r_0 being the radius of the cylindrical part of the penetrator.

We simulate all of the penetration tests reported in Tables 1 and 2 of Forrestal et al. [5] involving the nearly normal impact of hemispherical nosed steel rods onto aluminum targets. They also showed that the power law constitutive relation

$$\sigma = \sigma_0 \left(\frac{\psi}{\psi_0} \right)^n \tag{6}$$

with $\sigma_0 = 276\,\text{MPa}$, $n = 0.051$, $\psi_0 = 0.004$ and ψ interpreted as the strain modelled well the quasistatic stress-strain curve for the 6061 – T651 aluminum target material. Since aluminum alloys do not exhibit much strain-rate hardening, here we have set

$$b = 10\,000\,\text{sec}, \qquad m = 0.01, \qquad v = 0.001\,53/^\circ\text{C}, \tag{7.1}$$

to account for thermal softening and weak strain-rate sensitivity of the material. We have taken υ equal to the reciprocal of the temperature of the aluminum alloy, and assigned the following values to other material parameters:

$$\varrho_0 = 2710\,\mathrm{kg/m^3}, \quad A = 68.9\,\mathrm{GPa}, \quad B = 0, \quad k = 120\,\mathrm{Wm^{-1}\,{}^\circ C^{-1}},$$
$$c = 875\,\mathrm{Jkg^{-1}\,{}^\circ C^{-1}}, \quad \theta_a = 22\,{}^\circ\mathrm{C}, \quad h = 20\,\mathrm{Wm^{-2}\,{}^\circ C^{-1}}, \quad \mu = 0.12, \quad \beta = 1.5. \tag{7.2}$$

According to our constitutive relations (3.2) and (3.3), when $\theta = 1/\upsilon$ = melting temperature of the material, $\mu = 0$, the material behaves like an ideal fluid, and cannot support any shear stresses. In order to alleviate this problem, Eq. (3.3) was modified to

$$2\mu = \frac{\sigma_0}{\sqrt{3}\,I}\left(\frac{\psi}{\psi_0}\right)^n (1 + bI)^m (1 - \nu\theta), \quad \theta \leqq 0.955\,\theta_m, \tag{8.1}$$

$$= \frac{0.045\sigma_0}{\sqrt{3}\,I}\left(\frac{\psi}{\psi_0}\right)^n (1 + bI)^m, \quad \theta > 0.955\,\theta_m, \tag{8.2}$$

where θ_m equals the melting temperature of the target material. We note that the numerical simulations by Chen [3] of penetration tests involving conical-nosed penetrators, and the cavity expansion model of Forrestal et al. [5] do not consider thermal softening of the material. However, Chen and Batra [21] have shown that thermal softening influences strongly target's deformations.

3.1 *Results for a hemispherical-nosed penetrator*

Figure 2 exhibits the computed depth of penetration both with and without the consideration of frictional forces at the target/penetrator interface, and the test values from Tables 1 and 2 of Forrestal et al. [5] for $r_0 = 2.54$ mm and 3.555 mm. The abscissa equals the non-dimensional number $\alpha = \varrho_t v_0^2/\sigma_0$ sometimes also referred to as the damage number [27]. Higher values of

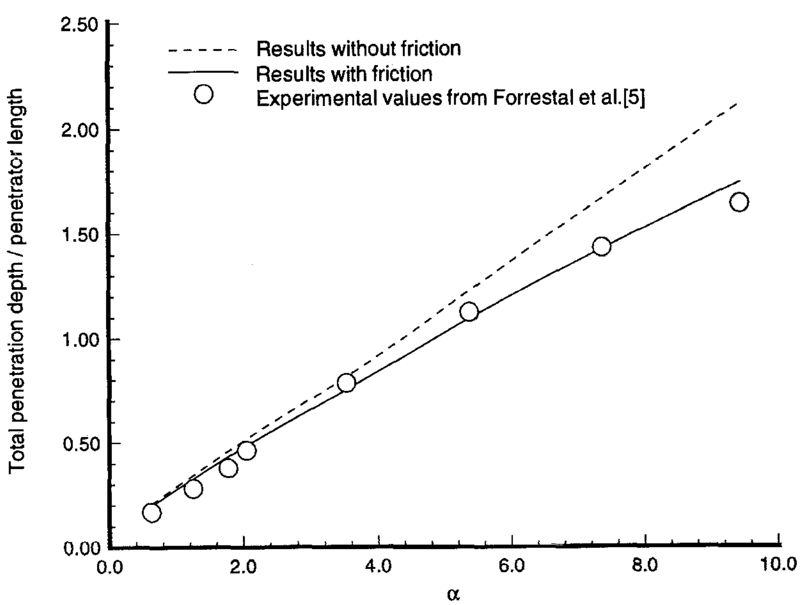

Fig. 2a

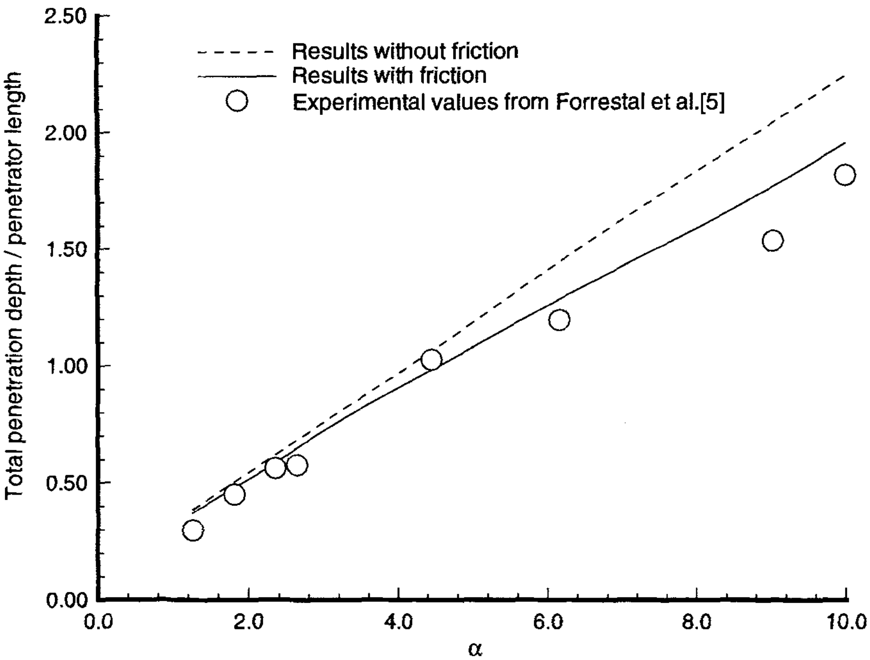

Fig. 2b

Fig. 2. Normalized penetration depth vs. the non-dimensional number $\alpha = \varrho_t v_0^2/\sigma_o$. **a** Penetrator radius $r_0 = 2.54$ mm, **b** $r_0 = 3.555$ mm

α are expected to result in more intense plastic deformations of the target. The plotted results evince that the depth of penetration computed by considering the frictional force at the target/penetrator interface matches well with that observed experimentally. For a striking speed of 1 km/s, the consideration of frictional forces reduces the penetration depth by about 12%, and the difference between the computed penetration depths with and without the consideration of frictional forces decreases with a decrease in the striking speed of the penetrator. It could at least partly be due to the longer duration of the penetration process at higher striking speeds. It is coincidental that $\mu = 0.12$ and $\beta = 1.5$, determined by Chen and Batra [4] by ensuring that the distribution of the tangential traction on the penetrator nose surface computed from the finite element solution of the steady state penetration problem and from the boundary layer theory match with each other, yield penetration depths very close to test values. One will expect that the values of μ and β depend upon the penetrator and target materials. Results plotted in Fig. 2 suggest that $\mu = 0.12$ and $\beta = 1.5$ are reasonably good for a steel penetrator and aluminum target as far as the total penetration depth is concerned.

Unless otherwise specified results presented below are for a 3.555 mm diameter steel-penetrator of mass 23.32 g striking at normal incidence an aluminum target with a speed of 1.009 km/s.

Figures 3a–c depict the geometry of the tunnel produced in the target when the penetrator speed has been reduced to 79.69%, 60.50%, and 30.67% of the initial striking speed. It is clear that the tunnel shape near the entrance region stays unaltered during the time the penetrator speed decreases from 79.69% to 30.67% of the initial striking speed. More material ahead of the penetrator nose than on its sides has been deformed severely, and the size of this intensely deforming region equals approximately twice the penetrator diameter.

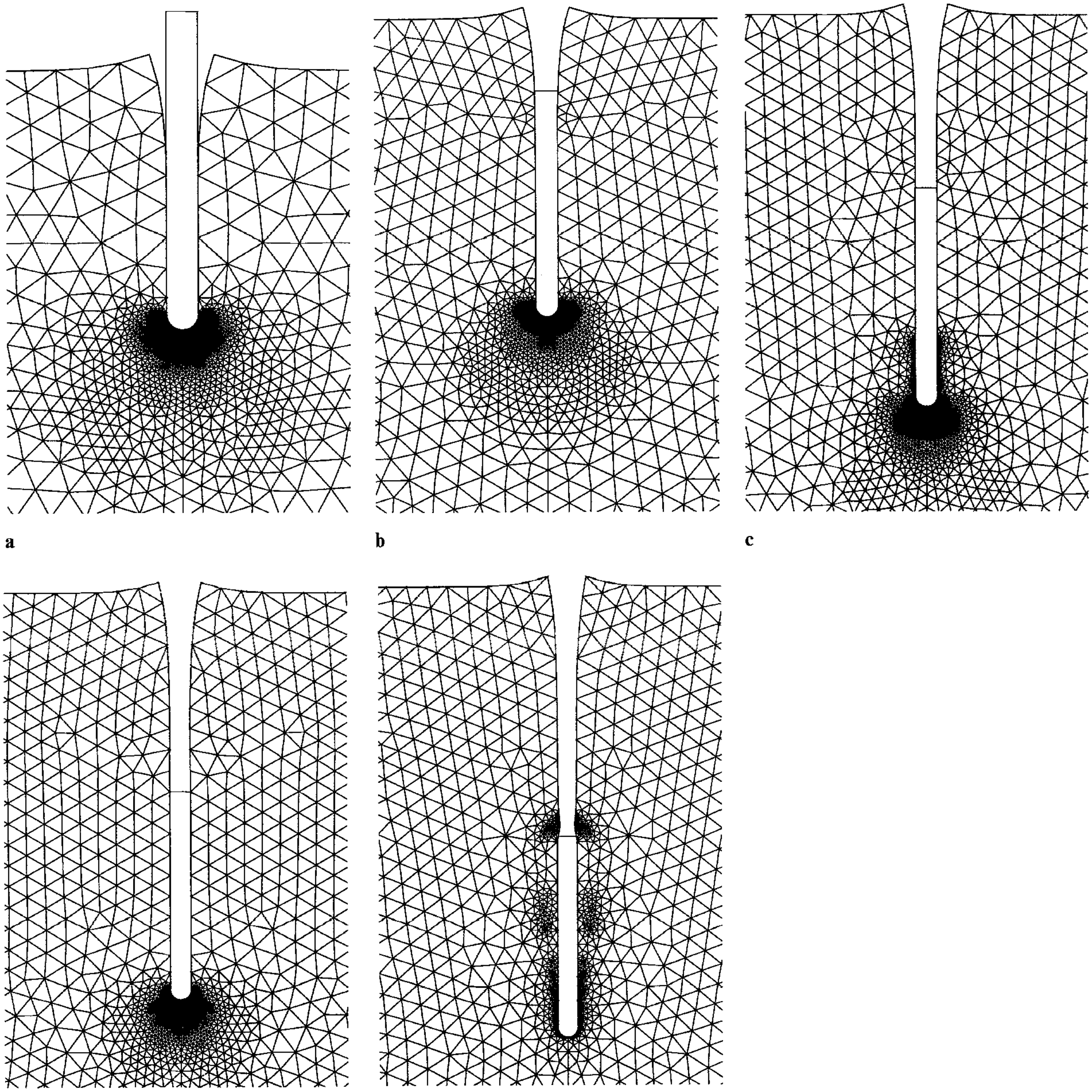

a b c d e

Fig. 3. Tunnel shapes with $\mu = 0.12$ when the penetrator speed has been reduced to **a** 0.7969, **b** 0.6050, and **c** 0.3067 times the initial speed of 1.009 km/s. Tunnel shapes at the end of the penetration process for $\mu = 0.12$ and 0.0 are given in **d** and **e** respectively

A comparison of these tunnel shapes with those reported in Figs. 5a–d of Chapter 3 of Chen's doctoral dissertation [28] suggests that for the case of a smooth target/penetrator interface more material on the sides of the interface is deformed severely as compared to that in the present case. When frictional effects are considered, the size of the severely deforming region ahead of the penetrator barely changes with time. This could be due to the retardation of the relative movement of the target material along the target/penetrator interface. Thus it will hinder

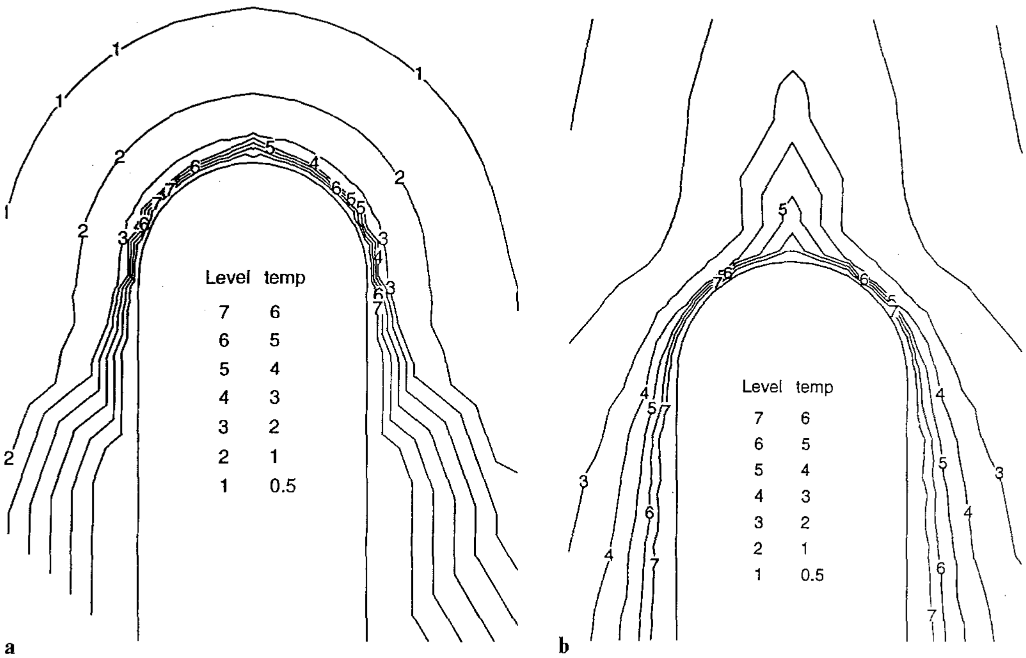

Fig. 4. Contours of temperature rise at the end of the penetration process for **a** $\mu = 0.12$ and **b** $\mu = 0.0$

the target material ahead of the penetrator nose from flowing backwards along the target/penetrator interface. The final shapes of the tunnels produced for the cases of nonzero and zero values of the coefficient of friction are shown in Figs. 3 d, e, respectively. These plots indicate that no narrowing down of the tunnel shape near the end of the penetrator surface occurs when frictional forces are accounted for.

The contours of temperature rise in the target region close to the penetrator surface at the end of the penetration process are plotted in Figs. 4 a, b for $\mu = 0.12$ and $\mu = 0.0$, respectively. Near the nose tip the temperature gradient is quite high for the case with friction as compared to that without friction. Also the temperature contours are essentially parallel to the nose surface when frictional effects are considered, but project far deeper into the target material ahead of the penetrator nose tip for the case of the smooth target/penetrator interface. Thus, more of the target material ahead of the penetrator nose tip is heated up significantly when frictional effects are ignored as compared to that when they are accounted for. Also the thickness of the molten target material along the target/penetrator interface is smaller for the case of the rough target/penetrator interface as compared to that for the smooth interface.

The contours of the hydrostatic pressure and the internal variable ψ in the deforming target region when the penetrator speed has been reduced to 60.5% of its initial striking speed of 1.009 km/s are plotted in Figs. 5 a, b for $\mu = 0.12$ and $\mu = 0.0$. Since the internal variable ψ is a measure of the plastic strain, it is clear that most severe deformations of the target material are concentrated within a narrow layer along the penetrator nose surface. That contours of ψ are very similar to those of the temperature rise follow from the observation that equations governing their evolution are essentially alike since the nondimensional thermal diffusivity is extremely small. It seems that the contours of the hydrostatic pressure are unaffected by the value of μ.

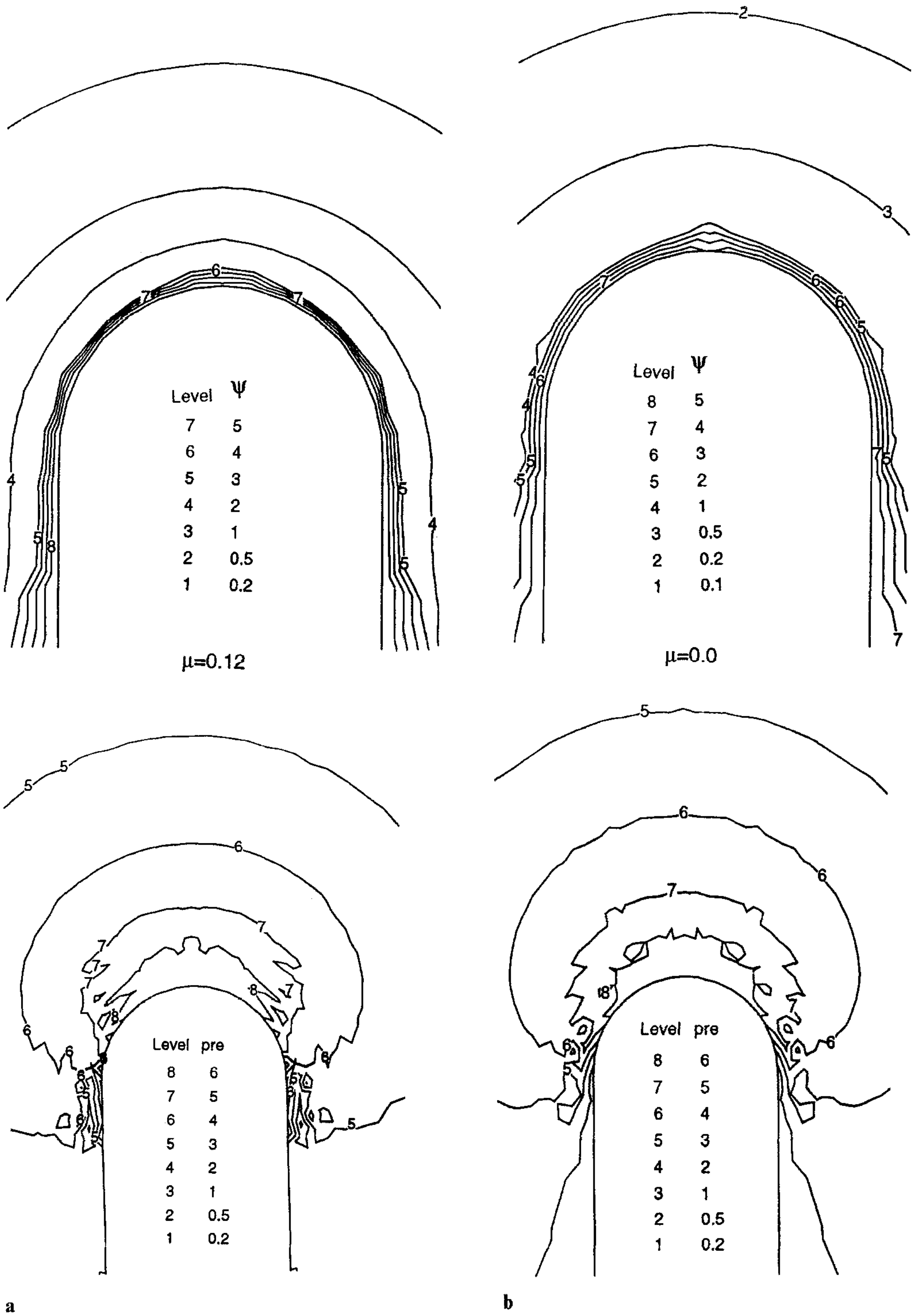

Fig. 5. Contours in the deforming target region of the hydrostatic pressure and the internal variable ψ when the penetrator speed has been reduced to 60% of the initial striking speed of 1.009 km/s **a** with and **b** without frictional effects

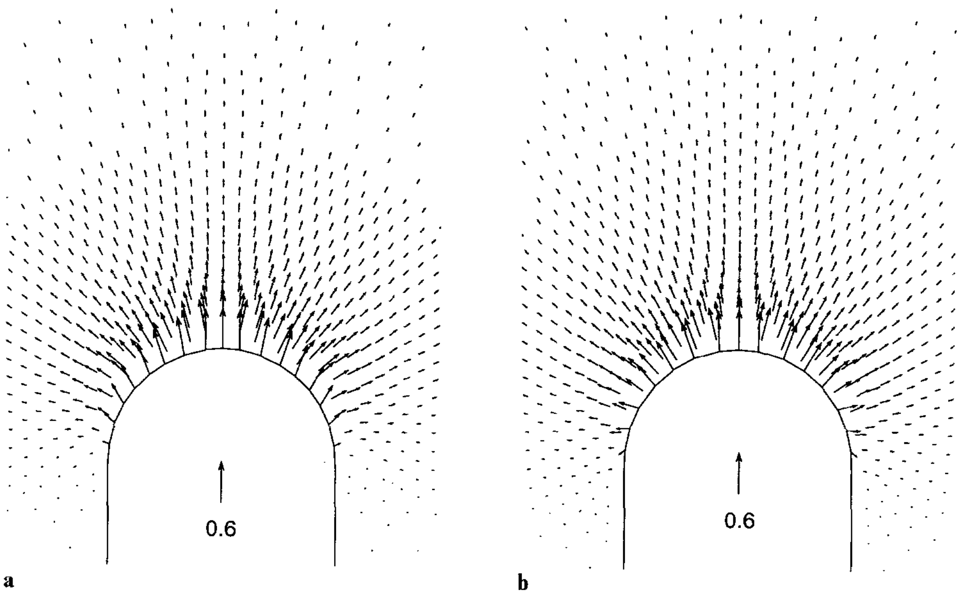

Fig. 6. Velocity field in the deforming target region adjacent to the penetrator/target interface for **a** $\mu = 0.12$ and **b** $\mu = 0.0$ when the penetrator speed has been reduced to nearly 60% of the striking speed

Figures 6a, b exhibit respectively for $\mu = 0.12$ and 0.0 the velocity field in the deforming target region adjacent to the target/penetrator interface when the penetrator speed has been reduced to nearly 60% of the initial striking speed. Whereas for $\mu = 0.0$ the axial component of the velocity of target particles abutting the penetrator surface near its nose periphery points backwards, that for $\mu = 0.12$ points forward. The angle between the velocity vector and the axial direction for similarly situated target particles on the nose periphery is *less* for $\mu = 0.12$ as compared to that for $\mu = 0$. Note that for the latter case target particles are free to slide on the penetrator surface.

3.2 Results for different values of μ

For the steady state phase of the penetration problem Chen and Batra [4] found that the values of μ affect significantly deformations of the target material adjoining the penetrator nose. Here we study the effect of the value of μ on the entire penetration process. Since the effect of the frictional force is more evident for higher striking speeds, we select the highest striking speeds of 980 m/s and 1.009 km/s in Tables 1 and 2 of Forrestal et al. for penetrator rods with shank radii of 2.54 and 3.555 mm. Figure 7 shows the dependence of the penetration depth upon μ for values of μ between 0 and 0.4. In each case the penetration depth decreases rapidly when μ is increased from 0 to 0.11 and then decreases rather slowly. The initial decrease in penetration depth is 17% and 13% for penetrators with $r_0 = 2.54$ and 3.555 mm respectively. For the two different penetrators considered, the experimentally computed penetration depth corresponds to $\mu = 0.295$. It is very likely that the dependence of the penetration depth upon μ is also influenced by the postulated form (4.3) of the frictional force.

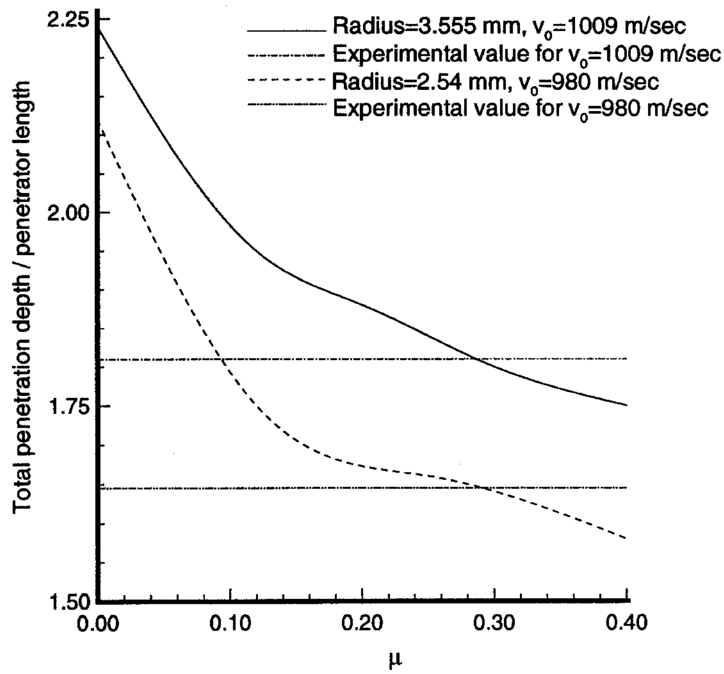

Fig. 7. Dependence of penetration depth upon μ for (i) penetrator radius = 3.555 mm, striking speed = 1.009 km/s (ii) penetrator radius = 2.54 mm, striking speed = 980 m/s

Figures 8a, b depict respectively the time histories of the non-dimensional axial resisting force experienced by the penetrator, penetrator position and its speed for different values of μ. The axial resisting force is nondimensionalized by $\pi r_0{}^2\sigma_0$, time by v_0/r_0, penetrator speed by v_0, and the penetrator position by its length. Here σ_0 equals the yield stress of the target material in a quasistatic simple compression test. In the beginning the resisting force is minimally affected by the value of μ. However, after about 10% of the duration of the penetration process, the resisting force gradually increases to about 10% higher than that computed without the consideration of the frictional force. This increase in the resting force is caused by the tangential traction exerted by the deforming target material on the penetrator surface. The normal traction on the target/penetrator interface is dominated by the hydrostatic pressure which is affected very little by the consideration of frictional forces. As expected, an increase in the value of μ increases the axial resisting force and thus decelerates the penetrator quicker. For the steady penetration problem, Chen and Batra [4] found that the axial resisting force depended moderately upon μ. The oscillations in the axial resisting force are probably due to high frequency oscillations resulting from multiple stress wave reflections from the top surface of the target. In our work we have not introduced any artificial viscosity to smoothen out these oscillations. The penetrator deceleration computed by Chen [3] also exhibited oscillatory behavior. However, the deceleration computed by differentiating twice with respect to time the penetrator position was found to be smoother than that computed directly from the numerical solution of the problem. For the case of the rough target/penetrator interface the penetrator speed decreases gradually to zero even towards the end of the penetration process. However, for smooth interface, the rate of decrease of the penetrator speed drops sharply towards the end of the penetration process. Because of the higher deceleration of the penetrator at larger values of μ, the total duration of the penetration process decreases as μ is increased.

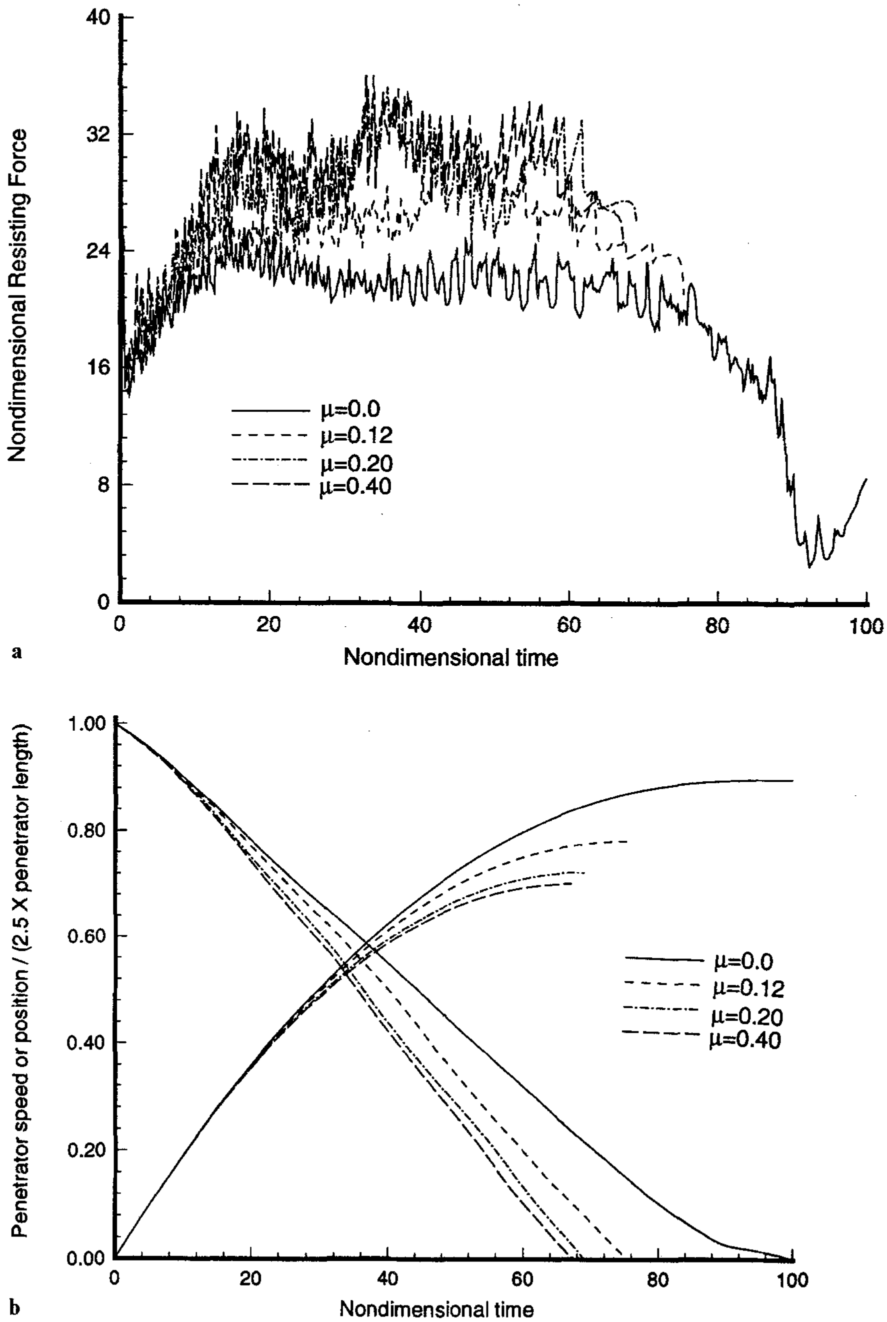

Fig. 8. Dependence upon μ of the time histories of the **a** non-dimensional axial resisting force, **b** penetrator position and penetrator speed

3.3 Results for different penetrator nose shapes

Figure 9 exhibits the dependence upon r_n/r_0 of the penetration depth and the total duration of the penetration process for $\mu = 0.12$ and initial striking speed $v_0 = 1.009$ km/s, and for $\mu = 0$ with $v_0 = 519$ m/s. Here r_n and r_0 equal the semi-major and semi-minor axes of the penetrator nose.

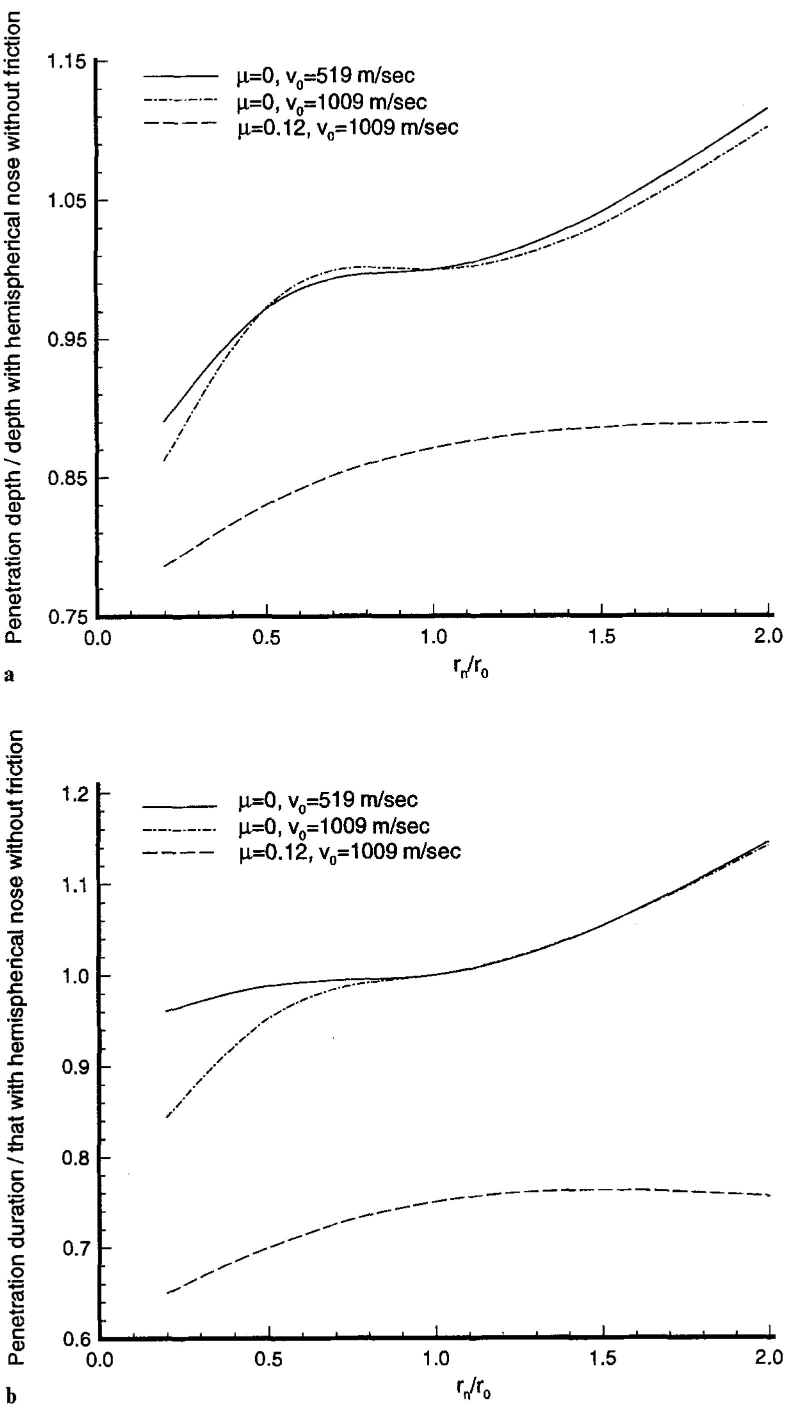

Fig. 9. Dependence upon r_n/r_0 of **a** the penetration depth and **b** the total duration of the penetration process for $\mu = 0$ and 0.12 at initial striking speed v_0 of 1.009 km/s, and for $\mu = 0.0$ at $v_0 = 519\,m/s$

Values of r_n/r_0 close to 0.2 imply a blunt nose, and those near 2 correspond to a moderately sharp nosed penetrator. In the plots of Fig. 9, the penetration time and the penetration depth are nondimensionalized with respect to their values for the smooth hemispherical nosed penetrator. For $\mu = 0$, the nose shape affects the normalized penetration depth and the duration of the

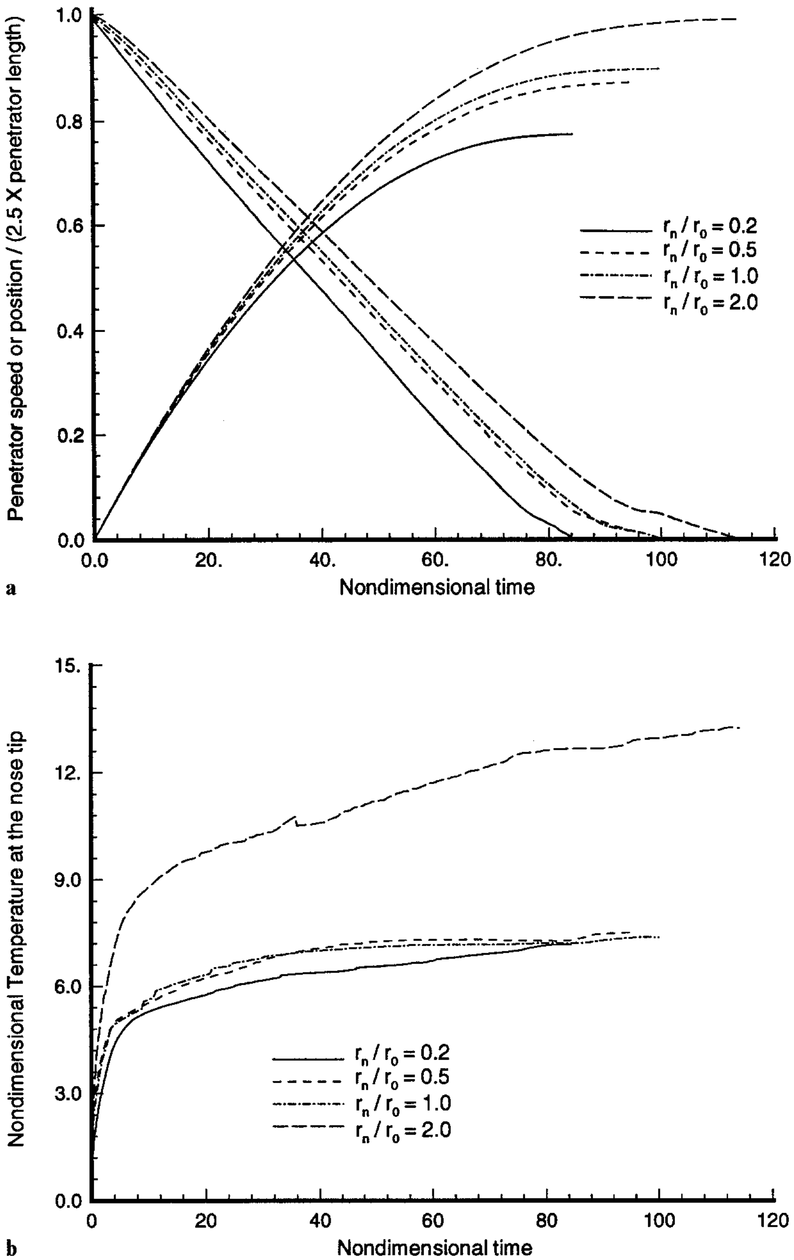

Fig. 10. Time histories for $\mu = 0$ and $v_0 = 1.009$ km/s of **a** the penetrator position, and the penetrator speed and **b** the temperature rise of a target particle abutting the penetrator nose tip

penetration process equally at the striking speeds of 519 m/s and 1.009 km/s, and the penetration depth and the duration of the penetration process decrease with a decrease in the value of r_n/r_0. When frictional forces with $\mu = 0.12$ are incorporated into the problem, the duration of the penetration process for $v_0 = 1.009$ km/s reaches an asymptotic value of 0.76 for $r_n/r_0 \geqq 1.25$. However, the penetration depth continues to increase, albeit slowly, with an increase in the value of r_n/r_0. For every value of r_n/r_0 considered, both the penetration depth and the duration of the penetration process decrease significantly when frictional forces are accounted for.

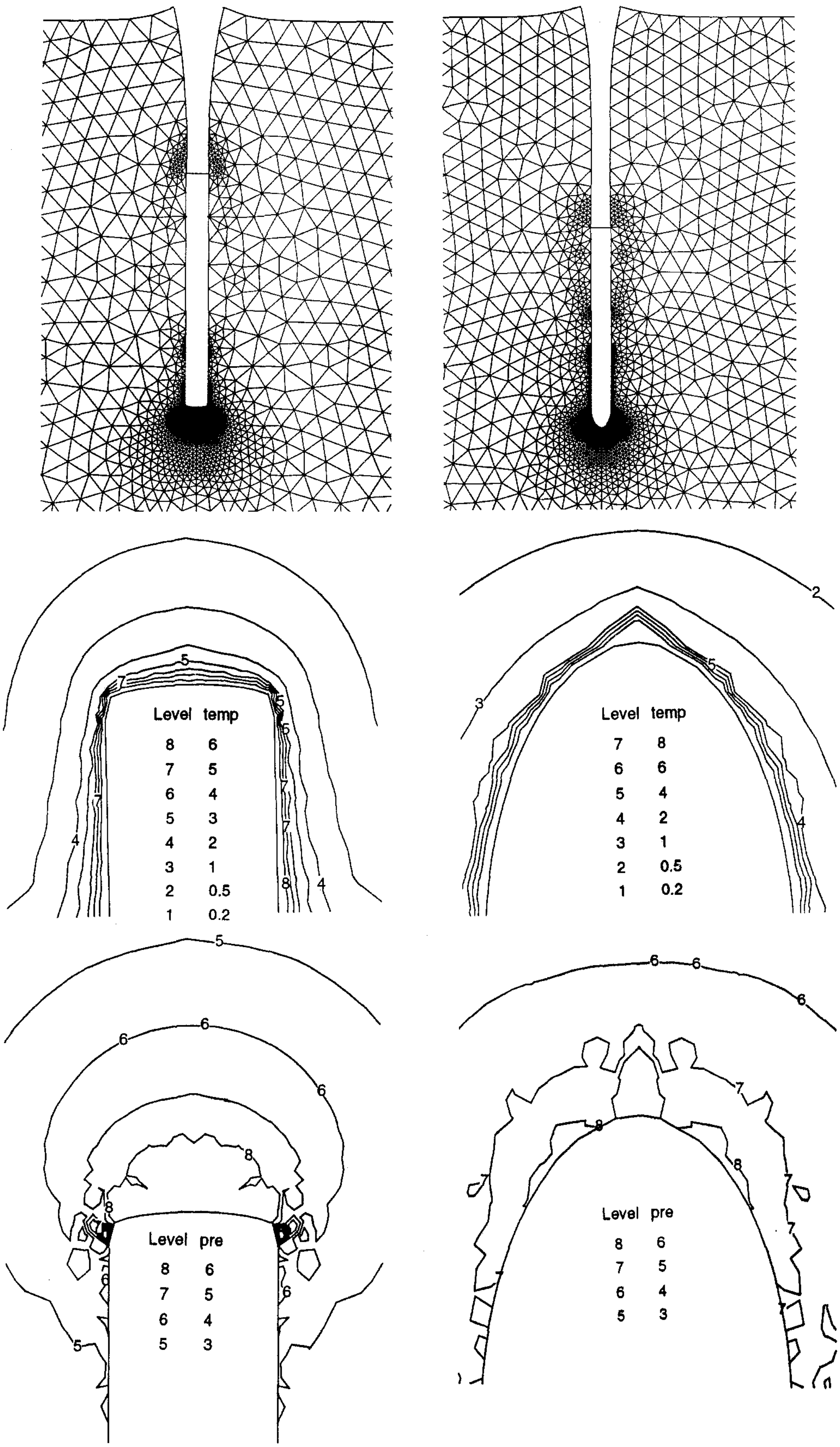

Level temp
8 6
7 5
6 4
5 3
4 2
3 1
2 0.5
1 0.2
Level temp
7 8
6 6
5 4
4 2
3 1
2 0.5
1 0.2
Level pre
8 6
7 5
6 4
5 3
Level pre
8 6
7 5
6 4
5 3

The time histories for different values of r_n/r_0 of the penetrator position, penetrator speed and the temperature rise of a target particle abutting the penetrator nose tip are depicted in Fig. 10. The computed results are for $\mu = 0$ and striking speed of 1.009 km/s. As expected, the penetrator with $r_n/r_0 = 0.2$ slows down most rapidly and that with $r_n/r_0 = 2.0$ most slowly. Towards the end of the penetration process, the deceleration of each one of these penetrators is smaller than that during the initial phase of the penetration process. Till the nondimensional time equals 4, penetrators with the four different nose shapes seem to have penetrated the target through the same amount suggesting thereby that initially the penetrator nose shape does not affect noticeably the penetration depth. At any other value of time, the penetrator with the blunt nose has penetrated through the least distance, and that with the sharpest nose through the greatest distance. This is because the axial resisting force acting on the blunt nosed penetrator is significantly more than that on the ellipsoidal nosed penetrator. The temperature of a target particle abutting the penetrator nose tip rises most rapidly for the ellipsoidal nosed penetrator and least rapidly for the blunt nosed penetrator. Recalling that the melting temperature of the target material equals 5.7, the target particle adjoining the penetrator nose tip melts soon after the target is struck when the penetrator nose is ellipsoidal. Since the temperature rise in the target is caused by the heat generated due to its being deformed plastically, and the heat lost due to conduction is negligibly small because of the low value of the thermal diffusivity and the small duration of the penetration process, one can conclude that severest deformations of the target material ahead of the penetrator nose tip occur for the ellipsoidal nosed penetrator.

The discretization of the target region adjoining the target/penetrator interface, contours of the temperature rise and of the hydrostatic pressure at an intermediate stage of the penetration process for a blunt nosed ($r_n/r_0 = 0.2$) penetrator and an ellipsoidal nosed ($r_n/r_0 = 2.0$) penetrator are plotted in Fig. 11. The penetrator speed has been reduced to 40% and 36% of the initial striking speed of 1.009 km/s for the blunt nosed and the ellipsoidal nosed penetrators. In each case frictional effects have been neglected. Recalling that the size of an element is inversely proportional to the value at its centroid of the second invariant of the deviatoric strain-rate tensor, these plots illustrate that the length of the target/penetrator interface spanning intensely deforming target material is more for the ellipsoidal nosed penetrator as compared to that for the blunt nosed penetrator. The shapes of the tunnel near the entrance to the target in the two cases are quite similar to each other. The intense plastic deformations ahead of the penetrator nose spread a little farther into the target for the ellipsoidal nosed penetrator as compared to that for the blunt nosed penetrator, and the shapes of these severely deforming regions are somewhat different in the two cases. The reason for plotting results at slightly different penetrator speeds is that the output from the computer code was obtained after a prescribed number of time steps. Contours of the temperature rise suggest that more of the target material ahead of the blunt nosed penetrator and on its sides has been heated up as compared to that for the ellipsoidal nosed penetrator. Thus intense plastic deformations spread farther for the blunt nosed penetrator than for the ellipsiodal nosed one. However, in each case a thin layer of the target material adjoining the target/penetrator interface melts. The contours of the hydrostatic pressure in the two cases reveal that the pressure does not drop to zero near the nose periphery. For the steady state penetration problems studied earlier by Batra and coworkers [18]–[20] the pressure at the nose

Fig. 11. The discretization of the target region adjoining the target/penetrator interface, contours of the temperature rise and of the hydrostatic pressure when penetrator speed equals approximately 0.4 v_0 for blunt nosed and ellipsoidal nosed penetrators

periphery essentially equalled zero for each nose shape studied. The intense deformations of the target were found to spread deeper into the target for the blunt nosed penetrator as compared to other nose shapes which agrees with the presently computed results.

For many of the penetration problems studied herein a thin layer of the target material adjacent to the target/penetrator interface melted and thus underwent severe plastic deformations. However, ahead of the penetrator nose no thin intensely deforming regions, usually known as adiabatic shear bands, were observed. This is probably due to the fact that no failure criterion has been induded in the problem formulation and that the target has been taken to be very thick.

4 Conclusions

We have studied the dynamic thermomechanical deformations of a very thick thermally softening viscoplastic target impacted at normal incidence by a cylindrical rod. The frictional force on the target/penetrator interface has been modelled by a velocity dependent relation proposed earlier by Chen and Batra [4]. Results for different values of the coefficient of friction and penetrator nose shapes have been computed and presented. The computed depth of penetration has been found to agree very well with the test values reported by Forrestal et al. [5]. For the same striking speed the penetration depth increases rapidly when r_n/r_0 is increased from 0.2 to about 0.7 and from 1.2 to 2.0, but quite slowly for r_n/r_0 between 0.7 and 1.2. However, when frictional effects are neglected, higher values of r_n/r_0 result in greater values of the penetration depth. At an intermediate stage of the penetration process, more of the target material ahead of the penetrator and on its sides has been deformed severely for a blunt nosed penetrator as compared to that for penetrators with other nose shapes. In each case a thin layer of the target material adjoining the target/penetrator interface essentially melted.

Acknowledgements

This work was supported by the U.S. Army Research Office Grant DAAL03-92-G-0315 to the University of Missouri-Rolla. Some of the computations were performed on the NSF sponsored supercomputer center at the University of Illinois in Urbana.

References

[1] Longcope, D. B., Forrestal, M. J.: Penetration of targets described by a Mohr-Coulomb failure criterion with a tension cutoff. J. Appl. Mech. **50**, 327–333 (1983).
[2] Forrestal, M. J.: Penetration into dry porous rock. Int. J. Solids Struct. **22**, 1485–1500 (1986).
[3] Chen, E. P.: Penetration into dry porous rock: a numerical study on sliding friction simulation. Theoret. and Appl. Fract. Mech. **11**, 135–141 (1989).
[4] Chen, X., Batra, R. C.: Effect of frictional force on the steady state axisymmetric deformations of a viscoplastic target. Acta Mech. **97**, 153–168 (1993).
[5] Forrestal, M. J., Brar, N. S.,Luk, V. K.: Penetration of strain-hardening targets with rigid spherical-nosed rods. J. Appl. Mech. **58**, 7–10 (1991).
[6] Backman, M. E., Goldsmith, W.: The mechanics of penetration of projectiles into targets. Int. J. Eng. Sci. **16**, 1–99 (1978).
[7] Wright, T. W., Frank, K.: Approaches to penetration problems. In: Impact: effects of fast transient loading (Ammann, W. J., Lui, W. K., Studer, J. A., Zimmermann, T. eds.). Rotterdam: Balkema, A. A. 1988.

[8] Anderson, C. E., Bodner, S. R.: The status of ballistic impact modelling. Proc. 3rd TACOM Armor Coordinating Conf., Feb. 17–19, 1987, Monterey, CA.
[9] Zukas, J. A., Nicholas, T., Swift, H. F., Greszczuk, L. B., Curran, D. R.: Impact dynamics. New York: Wiley-Interscience 1982.
[10] Blazynski, T. Z.: In: Materials at high strain rates (Blazynski, T. Z., ed). London New York: Elsevier 1987.
[11] MaCauley, M.:Introduction to impact engineering. London New York: Chapman and Hall 1987.
[12] Zukas, J. A.: High velocity impact dynamics. New York: Wiley 1990.
[13] Awerbuch, J., Bodner, S. R.: Analysis of the mechanics of perforation of projectiles in metallic plates. Int. J. Solids Struct. **10**, 671–684 (1974).
[14] Ravid, M., Bodner, S. R.: Dynamic perforation of viscoplastic plates by rigid projectiles. Int. J. Eng. Sci. **21**, 577–591 (1983).
[15] Ravid, M., Bodner, S. R., Holcman, I.: Analysis of very high speed impact. Int. J. Eng. Sci. **25**, 473–482 (1987).
[16] Forrestal, M. J., Okajima, K., Luk, V. K.: Penetration of 6061-T651 aluminum targets with rigid long rods. J. Appl. Mech. **55**, 755–760 (1988).
[17] Batra, R. C., Chen, X.: An approximate analysis of steady axisymmetric deformations of viscoplastic targets. Int. J. Eng. Sci. **28**, 1347–1358 (1990).
[18] Batra, R. C.: Steady state penetration of thermoviscoplastic targets. Comp. Mech. **3**, 1–12 (1988).
[19] Batra, R. C., Jayachandran, R.: Effect of constitutive models on steady state axisymmetric deformations of thermoelastic viscoplastic targets. Int. J. Impact Eng. **12**, 209–226 (1992).
[20] Batra R. C., Gobinath, T.: Steady state axisymmetric deformations of a thermoviscoplastic rod penetrating a thick thermoviscoplastic target. Int. J. Impact Eng. **11**, 1–31 (1991).
[21] Chen, X., Batra, R. C.: Deep penetration of thick thermoviscoplastic target by long rigid rods. (Submitted for publication).
[22] Batra, R. C., Lin, P. R.: Steady state axisymmetric deformations of a thermoviscoplastic rod striking a hemispherical rigid cavity. Int. J. Impact Eng. **8**, 99–113 (1989).
[23] Batra, R. C., Liu, D. S.: Adiabatic shear banding in plane strain problems. J. Appl. Mech. **56**, 527–534 (1989).
[24] Lysmer, J., Kuhlemeyer, R. L.: Finite dynamic model for infinite media. ASCE J. Eng. Mech. **95**, 859–877 (1969).
[25] Hallquist, J. O., Goudreau, G. L., Benson, D. J.: Sliding interfaces with contact-impact in large-scale Lagrangian computations. Comp. Meth. Appl. Mech. Eng. **51**, 107–137 (1985).
[26] Bathe, K. J.: Finite element procedures in engineering analysis. Englewood Cliffs: Prentice-Hall 1982.
[27] Bai, Y., Dodd, B.: Adiabatic shear localization: occurrence, theories, and applications. New York: Pergamon Press 1992.
[28] Chen, X.: Finite element analysis of axisymmetric deformations of thick thermoviscoplastic targets. Ph. D. dissertation, University of Missouri-Rolla 1993.

Authors' address: R. C. Batra* and X. Chen, Department of Mechanical and Aerospace Engineering and Engineering Mechanics, University of Missouri-Rolla, Rolla, MO 65401, U.S.A.
* *Permanent address*: Department of Engineering Science and Mechanics, Virginia Polytechnic Institute & State University. Blacksburg, VA 24061-0219, U.S.A.